

## Article

# Influence of the Gas Reaction Atmosphere on the Structure, Phase Composition, Functional Properties and Cytocompatibility of Porous Titanium–Nickel Alloys

Ekaterina Marchenko , Gulsharat Baigonakova \*  and Arina Shishelova

Laboratory of Superelastic Biointerfaces, National Research Tomsk State University, 36 Lenin Ave., 634045 Tomsk, Russia

\* Correspondence: gat27@mail.ru

**Abstract:** This work studies the effect that argon and nitrogen atmospheres have on the structure, phase composition, cytocompatibility, and functional properties of porous NiTi alloys obtained by self-propagating high-temperature synthesis. Porous alloys obtained in the nitrogen atmosphere (NiTi-(N)) are characterized by brittle interstitial phases  $Ti_4Ni_2O(N)$  and the appearance of a finely dispersed  $TiNi_3$  phase in comparison with the alloy obtained in an argon atmosphere (NiTi-(Ar)). An increase in the volume fraction of the  $Ti_4Ni_2O(N)$  phase as well as an increase in the content of nitrogen in the surface layer of the NiTi-(N) alloy favorably affects the surface cytocompatibility with bone marrow mesenchymal stem cells. It was found that the mechanisms of martensitic transformations in porous NiTi alloys under load and without load are different. It has been established that the mechanical characteristics of NiTi-(N) alloys are noticeably lower than those of NiTi-(Ar) alloys. Thus, according to the data obtained, porous NiTi-(N) alloys can be considered more biocompatible under low physiological load. However, it is necessary to increase their reversible deformation and tensile strength in order to use porous NiTi-(N) alloys under high physiological load.

**Keywords:** titanium–nickel; cytocompatibility; argon; nitrogen; martensitic transformation; tensile strength



**Citation:** Marchenko, E.; Baigonakova, G.; Shishelova, A. Influence of the Gas Reaction Atmosphere on the Structure, Phase Composition, Functional Properties and Cytocompatibility of Porous Titanium–Nickel Alloys. *Metals* **2022**, *12*, 2170. <https://doi.org/10.3390/met12122170>

Academic Editors: Chonghe Li, Li Liu and Jeff Th. M. De Hosson

Received: 12 October 2022

Accepted: 14 December 2022

Published: 16 December 2022

**Publisher's Note:** MDPI stays neutral with regard to jurisdictional claims in published maps and institutional affiliations.



**Copyright:** © 2022 by the authors. Licensee MDPI, Basel, Switzerland. This article is an open access article distributed under the terms and conditions of the Creative Commons Attribution (CC BY) license (<https://creativecommons.org/licenses/by/4.0/>).

## 1. Introduction

The successful integration and long-term functioning of porous implants in a living organism are determined by their biochemical and biomechanical compatibility with the bone tissues of the body. NiTi-based alloys occupy a special place among titanium alloys due to their shape memory and superelasticity effects. They have a number of features typical of mechanical and electrochemical behavior. High mechanical stability of titanium nickelide is achieved through the reversible martensitic transformation of the  $TiNi(B2) \leftrightarrow TiNi(B19')$  phase under physiological cyclic load [1–6]. Corrosion resistance of the porous TiNi alloys obtained by self-propagating synthesis (SHS) in an argon atmosphere is promoted by corrosion-resistant intermetallic oxycarbonitrides  $Ti_4Ni_2O$ , which comprise the protective surface layer of the alloy [7,8]. These features allow them to achieve higher biomechanical and biochemical compatibility with biological tissues in comparison with titanium alloys.

Porous titanium nickelide is synthesized in an inert atmosphere with a significant amount of gaseous impurities, which makes it possible to create conditions for gradient crystallization of intermetallic compounds on the alloy surface. The composition of the alloy surface improves the electrochemical passivity of the porous alloy. Nitrogen added to the protective gaseous medium in which SHS is carried out can increase the proportion of titanium nitrides in the surface layers of porous SHS-TiNi and, thus, increase its corrosion resistance and cytocompatibility. Titanium nitrides are known to have high corrosion

properties and biocompatibility, therefore, they are widely used as protective coatings for titanium implants [9,10].

In the existing studies of titanium nickelide, the main focus is on the influence which the heating rate [11], the synthesis start temperature [11–13], the size of the powder particles [14], and the pressure of the reaction gas [15] in the SHS have on the structure and properties of NiTi intermetallic compounds. However, the influence of the gas medium on the formation of surface intermetallic oxycarbonitrides has not been considered. The influence of gaseous atmosphere on the synthesis of the porous NiTi alloy has been considered in an alternative preparation method, called reaction sintering [16], where the authors concluded that the gaseous atmosphere has little effect on the phase composition and the amount of the  $Ti_2Ni$  phase formed in the matrix of the material. Therefore, the purpose of this work is to study the effect argon and nitrogen atmospheres have on the surface phase composition, cytocompatibility, fatigue strength, and functional properties of porous NiTi alloys during SHS.

## 2. Materials and Methods

Porous NiTi alloys were obtained by self-propagating high-temperature synthesis (SHS) in layer-by-layer combustion mode in argon and nitrogen atmospheres (Figure 1). The mixture of Ni50 + Ti50 powder (Polema, Moscow, RF) was placed into a quartz tube and then into the furnace (Tula-Term, Tula, RF). Before ignition, the samples were heated to 380 °C at a 15 °C/min heating rate. Argon and nitrogen flow into the reactor started at 0.05 MPa. To start the SHS reaction under the protective argon gas flow, the powder mixture was ignited by a nichrome filament at 380 °C. The synthesis starting temperature was selected experimentally to obtain a homogeneous isotropic structure. The samples obtained in argon and nitrogen atmospheres are designated NiTi-(Ar) and NiTi-(N), respectively.

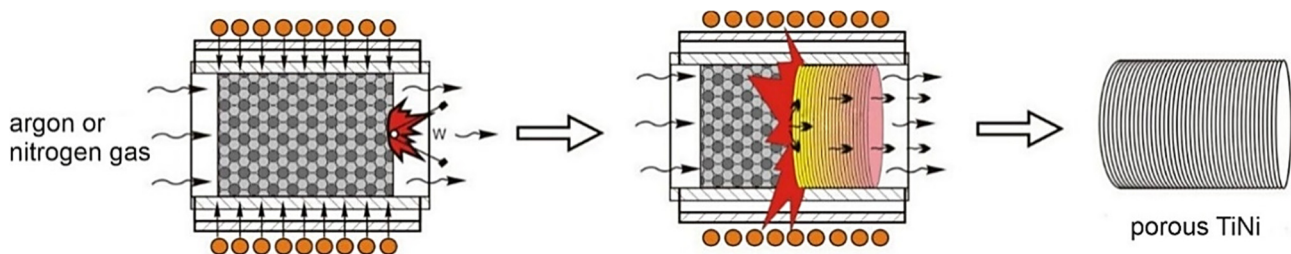


**Figure 1.** SHS scheme in a flow reactor for obtaining porous NiTi alloy.

The microstructure of porous alloys was analyzed using an Axiovert 200MAT optical microscope (Carl Zeiss, Jena, Germany). The secant method determined the average size of pores and inter-pore bridges. The study of porous sample structure was performed on a scanning electron microscope with an Axia ChemiSEM (Thermo Fisher Scientific, Waltham, MA, USA) equipped with an energy-dispersive X-ray spectrometer. The map of grain distribution was obtained by electron backscatter diffraction (EBSD) on a field emission scanning electron microscope TESCAN MIRA 3 LMU (TESCAN, Brno, Czech Republic), equipped with Oxford Instruments Ultim Max 40 EDS detector (Oxford Instruments, High Wycombe, UK). X-ray diffraction analysis was carried out on an XRD-6000 Cu  $K\alpha$ -radiation diffractometer (Shimadzu, Kyoto, Japan). The Powder Cell 2.4 program (W. Kraus & G. Nolze, Berlin, Germany) and the PDF-4+ database were used to promote full-profile analysis of X-ray images. The volume fractions of the phases were estimated by full-profile analysis based on calculations in relation to the intensities ratio of diffraction reflections using the Powder Cell 2.4 program and the PDF-4+ database. The lattice parameters and micro-stresses were calculated with precision using the Powder Cell 2.4 software.

Martensitic transformations were studied by differential scanning calorimetry (DSC) on a DSC 404 F3 calorimeter (NETZSCH Analyzing & Testing, Selb, Germany). The samples were heated from room temperature to 250 °C, then cooled to −150 °C and heated again

to 250 °C. To establish thermal equilibrium at the extreme points, the samples were kept isothermally for 5 min. The heating and cooling rates were 10 °C/min. The martensitic transformation temperatures were determined by the DSC peaks using the sloping line extension method.

The parameters of the shape memory effect (SME) and the intervals of its manifestation were studied under a constant load of 1 kg using an Instron 68TM-5 installation (Instron, Norwood, USA). Porous NiTi plates had a dimension of  $1 \times 7 \times 35 \text{ mm}^3$ . The test was carried out in a heating-cooling-heating cycle in the temperature range from +200 °C to −160 °C.

Uniaxial tension of porous NiTi sample plates  $20 \times 12 \times 5 \text{ mm}^3$  was carried out on a special tensile machine designed for precision tension in the column of a TESCAN MIRA II scanning electron microscope (TESCAN, Brno, Czech Republic). To increase the reliability of the results, two series of 10 samples have been tested. Stretching is carried out at the speed of 1  $\mu\text{m/s}$ . The fracture surface of the plates is examined using a TESCAN MIRA II scanning electron microscope.

To study the cytocompatibility of the surface of porous alloys, MCF-7 cells were cultured for 72 h under standard conditions at 37 °C, 5% CO<sub>2</sub>, and a humidified atmosphere. Complete culture medium consisted of DMEM/F12 (Paneco, RF, Tokyo, Japan) supplemented with 10% fetal bovine serum, 40  $\mu\text{g/mL}$  gentamicin, and 250 mg/l glutamine. Cells were visualized using double staining with acridine orange and ethidium bromide. The surface of the porous NiTi alloy with cells deposited was studied using an LSM-780NLO confocal laser scanning microscope (Carl Zeiss, Jena, Germany). The localization of live and dead cells was tracked by overlaying fluorescent images in the transmitted light mode; live cells were highlighted in green and dead cells were highlighted in red. The surface area of a porous sample and the area occupied by cells on the sample surface were measured with optical images from a confocal microscope. By comparing the measurements of these two areas, it was possible to obtain the percentage of cells covering the surface of the porous samples.

### 3. Results

The porous structure of NiTi-(Ar) and NiTi-(N) alloys is typical of porous materials if a liquid phase was involved in the obtaining process. The metal matrix is represented by a set of narrow and wide interpore bridges (Figure 2).

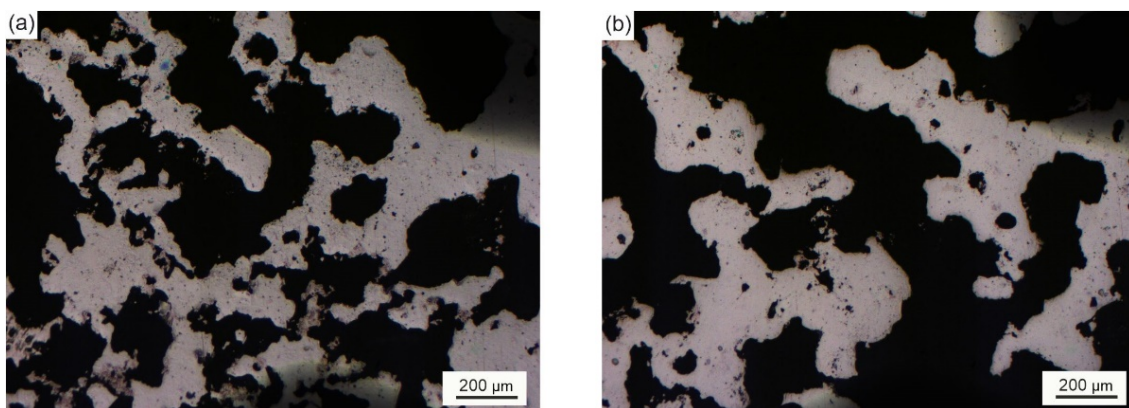


**Figure 2.** Optical images of the macrostructure of porous NiTi-(Ar) (a) and NiTi-(N) (b) alloys.

The analysis of the pore structure of the alloys showed that all materials are characterized by a unimodal pore size distribution. However, the average pore size for the NiTi-(Ar) alloy is about 205  $\mu\text{m}$  (Figure 3a), while for the NiTi-(N) alloy, the average pore size is 263  $\mu\text{m}$  (Figure 3b). The fact corresponds with the increase in the total porosity of these materials. The porosity of the NiTi-(Ar) alloy is about 60%; fine and medium pores are

more typical of the alloy. The NiTi-(N) alloy is characterized by large pores; its porosity reaches 67%.

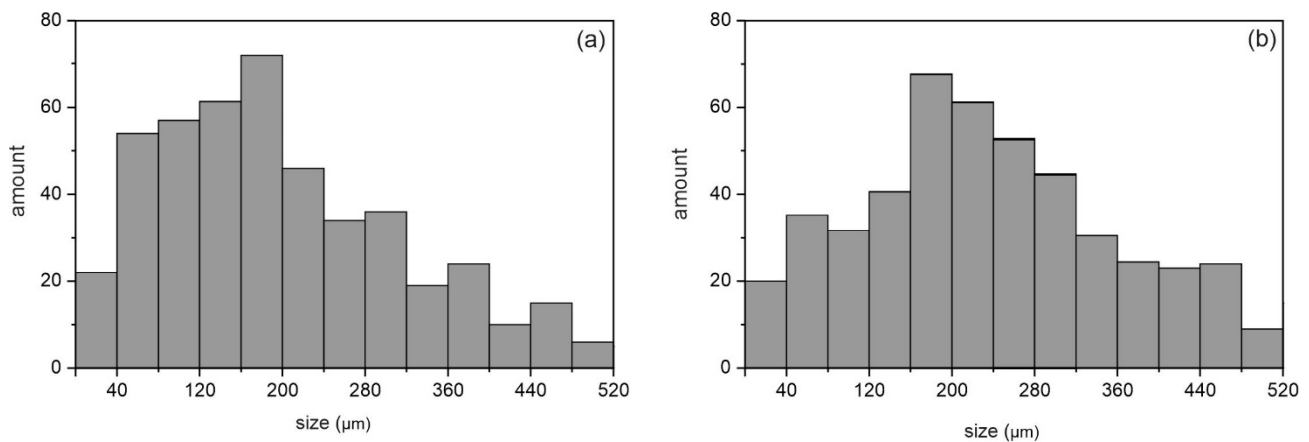


**Figure 3.** Pore size distribution histogram of porous NiTi-(Ar) (a) and NiTi-(N) (b) alloys obtained by the SHS.

The change in the gaseous medium in the alloy-obtaining process causes not only an increase in the average pore size, but also an increase in the thickness of interpore bridges, from 137 to 164 microns (Figure 4).

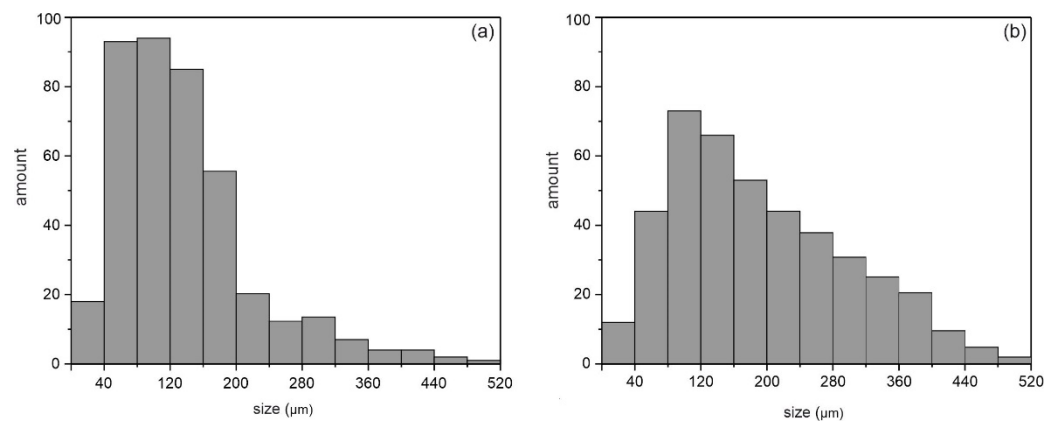


**Figure 4.** Size distribution histogram of interpore bridges of porous NiTi-(Ar) (a) and NiTi-(N) (b) alloys obtained by the SHS.

The comparative analysis of the phase composition of two polished NiTi-(Ar) and NiTi-(N) samples was carried out by X-ray diffraction analysis (Figure 5, Table 1). The main structural components of the porous NiTi-(Ar) alloy are intermetallics of the Ni–Ti system: austenite TiNi in modification B2 with the volume fraction of  $\approx 66.2$  vol.%, martensite TiNi in modification B19' with the volume fraction of  $\approx 9.4$  vol.% and a mixture of  $Ti_2Ni + Ti_4Ni_2O$  phases with the volume fraction of  $\approx 24.4$  vol.%. The NiTi-(N) alloy is characterized by the NiTi austenite phase in modification B2 with the volume fraction of  $\approx 55.8$  vol.%, NiTi martensite in modification B19' with the volume fraction of  $\approx 11.8$  vol.%, mixtures of phases  $Ti_2Ni + Ti_4Ni_2O(N)$  with the volume fraction of  $\approx 32.4$  vol.% and traces of the  $TiNi_3$  phase. Based on the data obtained, it can be seen that the content of martensite NiTi(B19') and the mixture of phases  $Ti_2Ni + Ti_4Ni_2O(N)$  is higher in the porous NiTi-(N) alloy than in NiTi-(Ar). The structural lines of the  $Ti_2Ni$  and  $Ti_4Ni_2O(N)$  phases cannot be distinguished in the X-ray diffraction pattern due to insignificant differences in their crystal lattices. All the detected intermetallic phases are completely crystalline.

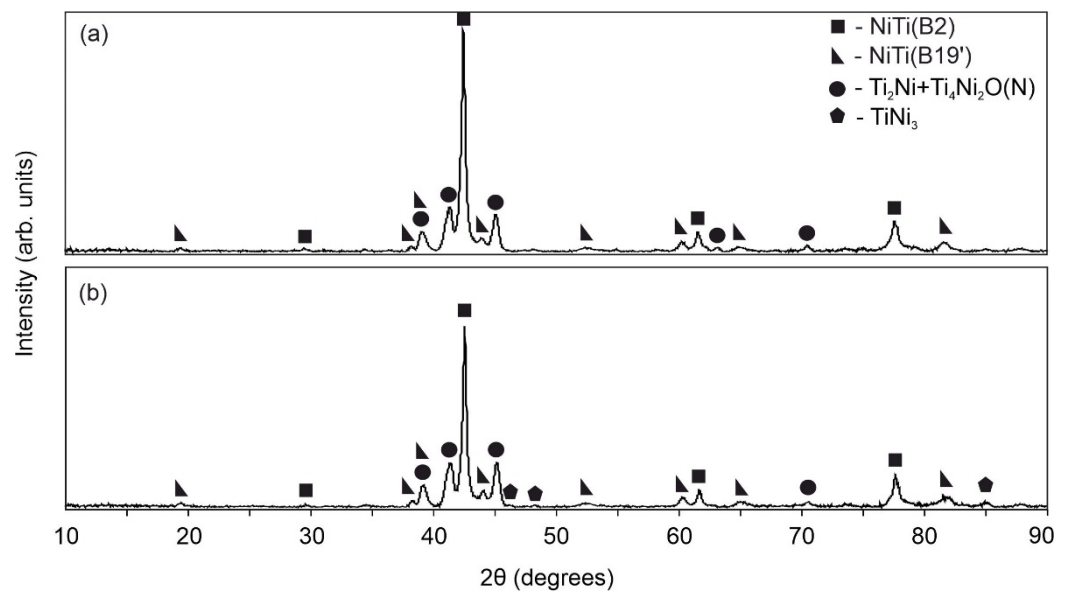


**Figure 5.** X-ray diffractograms of porous NiTi-(Ar) (a) and NiTi-(N) (b) samples obtained by the SHS.

**Table 1.** XRD data from the surface of porous NiTi-(Ar) and NiTi-(N) samples.

Sample	Phase	Vol. Fraction, vol.%	Lattice Parameter, Å	CSR, nm	$\Delta d/d \times 10^{-3}$
NiTi-(Ar)	NiTi (B2)	66.2	$a = 3.0169$	43	0.6
	NiTi (B19')	9.4	$a = 4.5470$ $b = 4.0784$ $c = 2.8848$ $\beta = 97$	20	5.6
	Ti <sub>2</sub> Ni + Ti <sub>4</sub> Ni <sub>2</sub> O	24.4	$a = 11.3852$	24	0.1
NiTi-(N)	NiTi (B2)	55.8	$a = 3.0167$	11	6.3
	NiTi (B19')	11.8	$a = 4.5768$ $b = 4.0697$ $c = 2.8908$ $\beta = 97$	17	3.1
	Ti <sub>2</sub> Ni + Ti <sub>4</sub> Ni <sub>2</sub> O (N)	32.4	$a = 11.3967$	24	0.8
	TiNi <sub>3</sub>	traces	-	-	-

Error in determination of the phase content  $\pm 2$  vol.%.

Table 1 lists the structural parameters of the unit cells of the discovered compounds based on NiTi: volume fraction, coherent scattering region (CSR) values and micro-stresses  $\Delta d/d$ . It can be seen that the stress of the main phase of the TiNi(B2) matrix is higher for the NiTi-(N) alloy. The value of the unit cell parameter of the B2 phase in the NiTi-(N) alloy is close to the value of NiTi-(Ar). In this case, the size of CSR blocks decreases from 43 nm to 11 nm. The features found are confirmed by the EBSD analysis data. The microstructural orientation maps show that the size of the NiTi crystallites in the porous NiTi-(Ar) alloy varies from 1 to 24  $\mu\text{m}$  (Figure 6). For the porous NiTi-(N) alloy, the size of crystallites in NiTi grains varies from 1 to 13  $\mu\text{m}$  (Figure 7). In addition to the NiTi, Ti, and Ti<sub>2</sub>Ni phases, a finely dispersed TiNi<sub>3</sub> phase was also found for the porous NiTi-(N) alloy. The TiNi<sub>3</sub> phase can cause additional stress in the matrix of the NiTi-(N) alloy and thereby reduce the reversible deformation. For these two types of samples, no prominent grain orientation is observed.

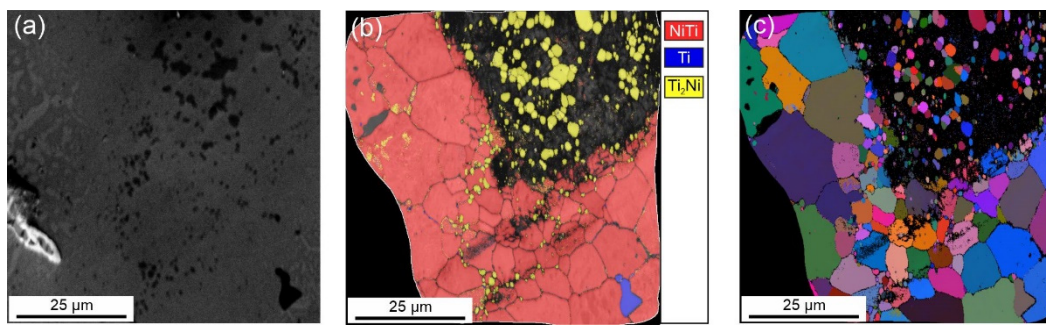


**Figure 6.** Orientation maps of crystals obtained on the cross section of the interpore bridge of the porous NiTi-(Ar) sample: (a) SEM image of the matrix of the porous NiTi-(Ar) sample, (b) phase map, (c) orientational color map at the Euler angle.

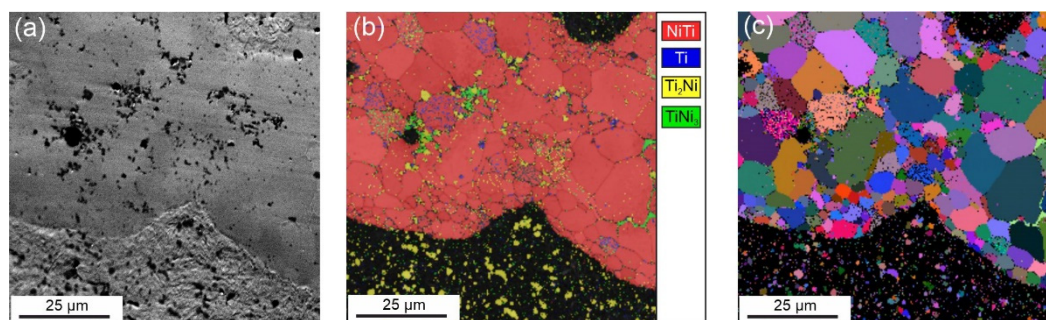


**Figure 7.** Orientation maps of crystals obtained on the cross section of the interpore bridge of the porous NiTi-(N) sample: (a) SEM image of the matrix of the porous NiTi-(N) sample, (b) phase map, (c) orientational color map at the Euler angle.

A certain amount of O, N, C in the composition of interstitial impurities was found in porous titanium nickelide alloys obtained both in an inert argon atmosphere and in a reactive nitrogen atmosphere. It can be explained by the fact that in any reactor there is always residual air containing oxygen and nitrogen, as well as residual carbon dioxide containing carbon and oxygen. Moreover, Ti and Ni powders contain adsorbed and dissolved impurities O, N, C. Chemisorption and reaction diffusion occurring at different stages of the alloy crystallization during SHS cause interstitial impurities O, N, C to form chemical compounds with metals and limited solid solutions [17,18].

In the Ni–Ti binary system, the  $Ti_2Ni$  intermetallic compound, more than other phases, is capable of dissolving light elements and forming the  $Ti_4Ni_2O(N)$  phase, which is stable up to the temperature of 1050 °C [19–21]. Impurity atoms O and N start diffusing at different values of activation energy, and for Ti the values are as follows: O/Ti 2.08–2.26 [22,23], N/Ti 2.32–2.94 [22]. Based on the state diagram and diffusion activation energy, it can be concluded that, regardless of the reaction atmosphere used, the amount of oxygen in the samples will be higher than the amount of nitrogen. The N impurity is maximally soluble in  $Ti_2Ni$  at 1050 °C, but the solubility of O in  $Ti_2Ni$  at 900 °C is much higher [19–21]. The cause of a more active dissolution of O in the  $Ti_2Ni$  phase in comparison with N is a lower activation energy of the oxygen diffusion.

According to the energy dispersive analysis data, in contrast to the porous NiTi-(Ar) sample, the NiTi-(N) alloy shows an increase in the N concentration in the surface layer (Figures 8 and 9). Local SEM-EDS analysis of the porous NiTi-(N) alloy showed the content of elements Ti (41 at. %), Ni (39 at. %), O (8 at. %), N (12 at. %) in the surface layer. For porous NiTi-(Ar) alloy-Ti (45 at. %), Ni (40 at. %), O (10 at. %), and N (5 at. %). Residual oxygen and nitrogen are always present in the reactor; therefore, in the NiTi-(Ar) alloy there is a small fraction of N incorporation into the  $Ti_4Ni_2O(N)$  surface layer.

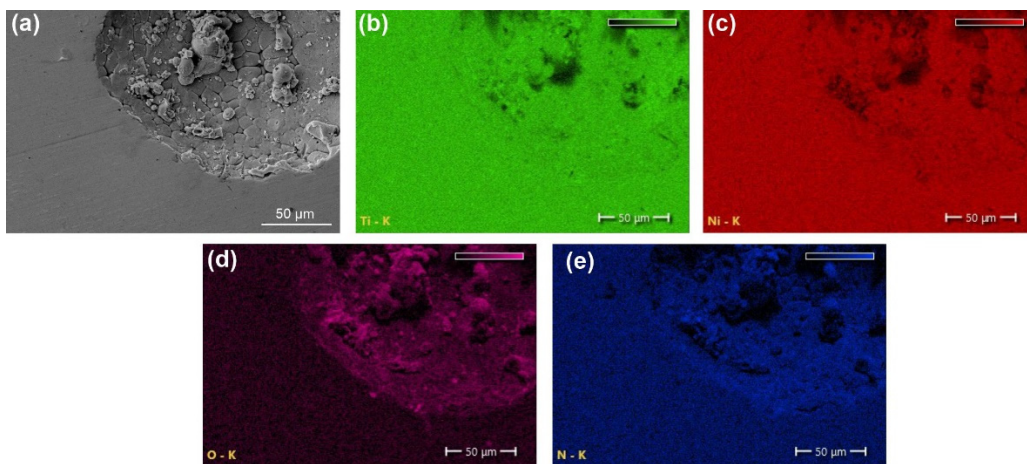


**Figure 8.** Energy-dispersive analysis of the interpore bridge of porous NiTi-(Ar) alloy: (a) SEM image, and (b) Ti, (c) Ni, (d) O, and (e) N maps.

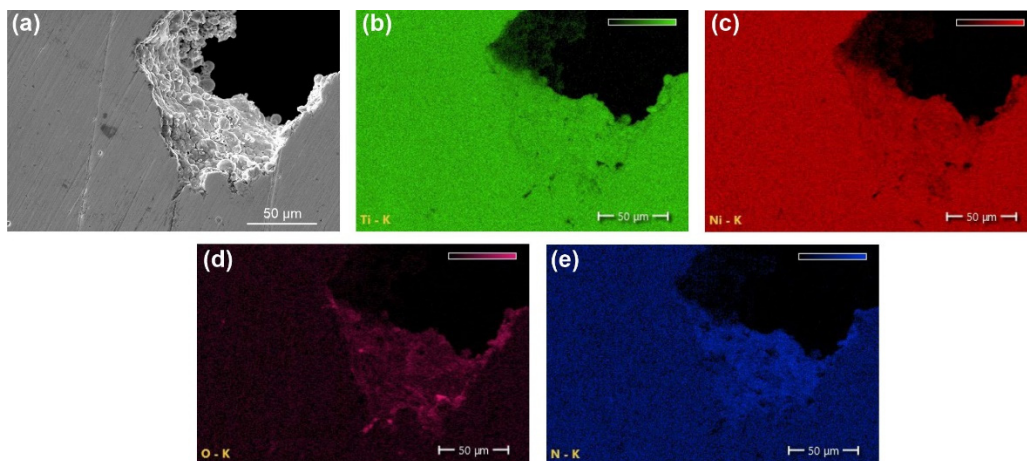


**Figure 9.** Energy-dispersive analysis of the interpore bridge of porous NiTi-(N) alloy: (a) SEM image, and (b) Ti, (c) Ni, (d) O, and (e) N maps.

The assertion of a higher biocompatibility of surface phases containing nitrides has been tested in *in vitro* experiments on bone marrow mesenchymal cells. Confocal microscopy on NiTi-(Ar) and NiTi-(N) samples with precipitated cells has shown a homogeneous distribution of cell mass (Figure 10). The percentage of surface cell coverage for NiTi-(N) is high and makes up 90% (Figure 10b), in contrast to NiTi-(Ar) with 75% coverage (Figure 10a). From the data obtained, it can be concluded that the surface layer of the NiTi-(N) alloy is more cytocompatible and, as a result, has a favorable effect on cell adhesion and proliferation. The found structural features of the surface are favorable for creating implants, but it is necessary to find out whether intermetallic oxynitrides affect martensitic transformations and the mechanical properties of porous titanium nickelide alloys.

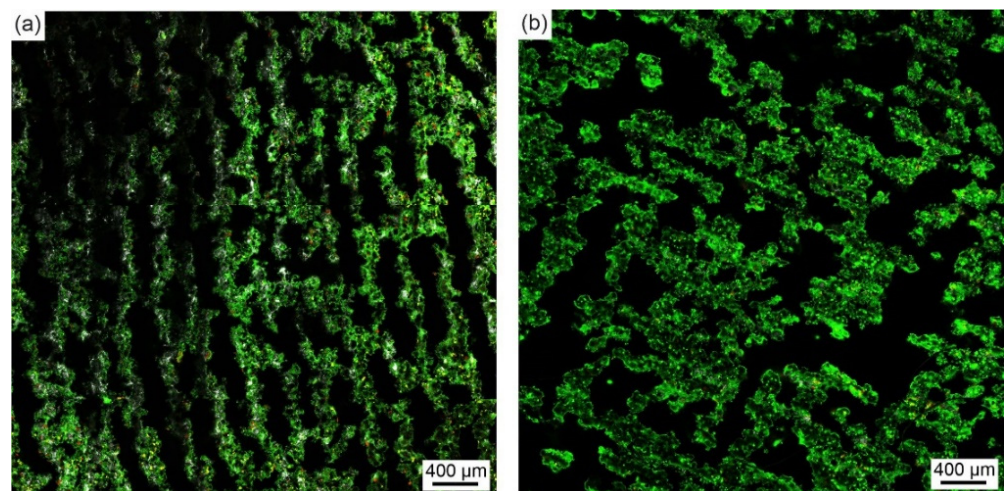


**Figure 10.** In vitro distribution of MCF-7 cell mass on the surface of porous NiTi-(Ar) (a) and NiTi-(N) (b) alloys obtained by the SHS.

Studies of the martensitic transformation without load (Figure 11) and under load (Figure 12) were carried out using two methods such as DSC and the temperature dependences of the accumulation and recovery of deformation during the SME. According to the calorimetric curves of porous NiTi-(Ar) and NiTi-(N) alloys, a one-stage martensitic transformation  $B2 \leftrightarrow B19'$  was established during cooling and heating without load (Figure 11). Table 2 shows the characteristic transformation temperatures  $M_s$ ,  $M_f$ ,  $A_s$ ,  $A_f$  and the enthalpy change  $\Delta H^{M \rightarrow A}$ ,  $\Delta H^{A \rightarrow M}$ . It can be seen from the temperature values that the gaseous atmosphere does not affect the characteristic martensitic transformation temperatures during cooling and heating. The stability of phase transformation temperatures is ensured by the austenitic phase B2. The presented temperatures of martensitic transformations  $M_s$ ,  $M_f$ ,  $A_s$ ,  $A_f$  correspond with the results obtained by other authors who studied SHS-NiTi alloys [24,25].

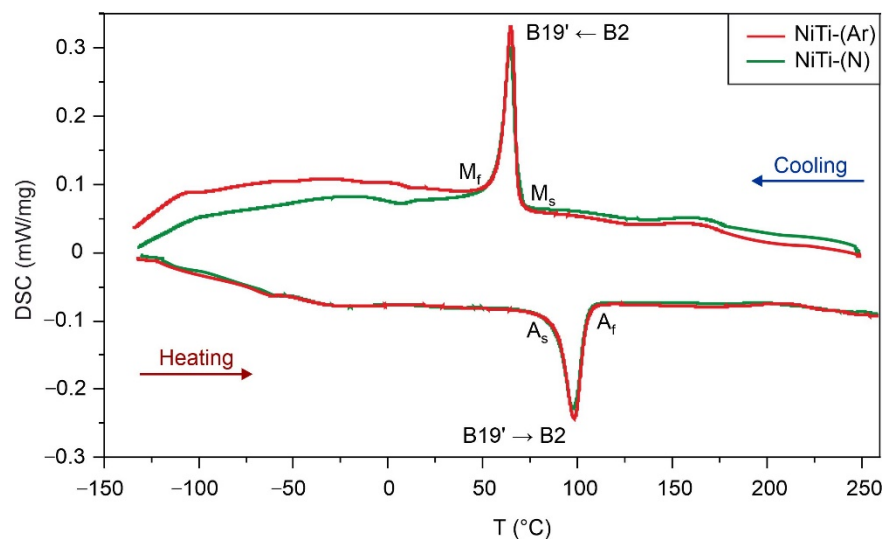


**Figure 11.** DSC curves of NiTi-(Ar) and NiTi-(N) samples.

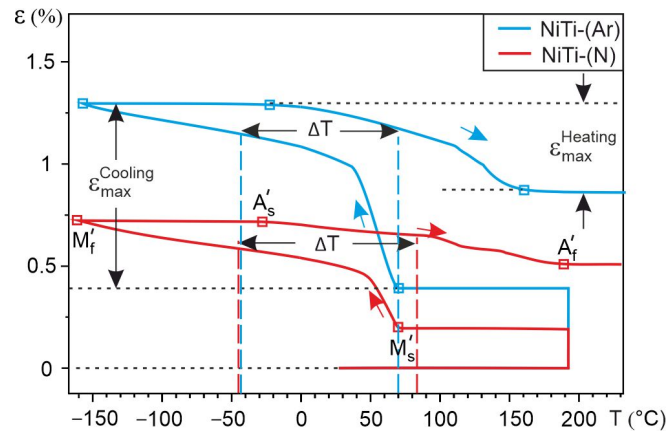


**Figure 12.** Temperature dependencies of accumulation and recovery of deformation during SME of porous TiNi-(Ar) and TiNi-(N) alloys.

**Table 2.** DSC transformation temperatures and enthalpies of porous NiTi-(Ar) and NiTi-(N) samples.

Sample	$M_s, ^\circ\text{C}$	$M_f, ^\circ\text{C}$	$A_s, ^\circ\text{C}$	$A_f, ^\circ\text{C}$	$\Delta H^{A \rightarrow M}, \text{J/g}$	$\Delta H^{M \rightarrow A}, \text{J/g}$
NiTi-(Ar)	69	59	90	105	−12.54	10.95
NiTi-(N)	69	58	88	105	−11.65	10.67

The main thermodynamic parameters were calculated to evaluate the thermodynamics of martensitic transformations for two alloys. The equilibrium temperature of the martensitic and austenitic phases  $T_0$ , at which the Gibbs free energies of the two phases are equal [26], was calculated by the formula:

$$\Delta G^{M \rightarrow A}(T_0) = G^A(T_0) - G^M(T_0) = (H^A - T_0 S^A) - (H^M - T_0 S^M) = 0 \quad (1)$$

$$T_0 = \frac{\Delta H^{M \rightarrow A}}{\Delta S^{M \rightarrow A}} = \frac{M_s + A_f}{2} \quad (2)$$

$$\Delta S^{M \rightarrow A} = \frac{\Delta H^{M \rightarrow A}}{T_0} \quad (3)$$

The driving force of martensite was determined by the formula [26]:

$$\Delta G^{A \rightarrow M}(M_s) = \Delta G^{M \rightarrow A}(T_0) - \Delta G^{M \rightarrow A}(M_s) = -(T_0 - M_s) \Delta S^{M \rightarrow A} \quad (4)$$

Based on the data obtained (Table 2), the following thermodynamic parameters were calculated:  $T_0$ —equilibrium temperature of the martensitic and austenitic phases;  $\Delta S^{A \rightarrow M}$ ,  $\Delta S^{M \rightarrow A}$  are entropy changes during the phase transformation;  $\Delta G^{A \rightarrow M}(M_s)$  is the driving force of martensite nucleation. The obtained values are listed in Table 3.

**Table 3.** Calculated values of thermodynamic parameters for porous NiTi-(Ar) and NiTi-(N) samples obtained by the SHS.

Sample	$T_0, ^\circ\text{C}$	$\Delta S^{A \rightarrow M}, \text{J/gK}$	$\Delta S^{M \rightarrow A}, \text{J/gK}$	$\Delta G^{A \rightarrow M}, \text{J/g}$
NiTi-(Ar)	87	−0.035	0.03	−0.54
NiTi-(N)	87	−0.032	0.029	−0.52

The calculated values of thermodynamic parameters during martensitic transformation of porous NiTi-(Ar) and NiTi-(N) alloys without load are close, which indicates the invariance of the matrix chemical composition with a change in the gaseous atmosphere.

Martensitic transformations were studied under load with the shape memory effect (SME). The temperature dependences of the accumulation and recovery of deformation during the SME of porous NiTi-(Ar) and NiTi-(N) alloys are shown in Figure 12. Based on the analysis of dependencies  $\varepsilon(T)$ , it was possible to determine the characteristic temperatures of martensitic transformation under load and shape memory parameters in porous NiTi-(Ar) and NiTi-(N) alloys (Table 4).

**Table 4.** SME parameters of porous NiTi-(Ar) and NiTi-(N) alloys.

Sample	$M'_{s'}$ , °C	$M'_{f'}$ , °C	$A'_{s'}$ , °C	$A'_{f'}$ , °C	$\varepsilon_{cool'}^{rev}$ %	$\varepsilon_{heat'}^{rev}$ %	$\Delta T$ , °C
NiTi-(Ar)	70	−158	−22	160	0.9	52	113
NiTi-(N)	70	−160	−28	190	0.51	59	126

Where,  $\varepsilon_{cool'}^{rev}$  % is the maximum accumulated deformation during cooling;  $\varepsilon_{heat'}^{rev}$  — maximum accumulated deformation during heating;  $M'_{s'}$ ,  $M'_{f'}$  are the temperatures of the beginning and the end of the direct martensitic transformation, respectively;  $A'_{s'}$ ,  $A'_{f'}$  are the temperatures of the beginning and the end of the reverse martensitic transformation, respectively;  $\Delta T$  is the temperature hysteresis of the SME.

While studying the SME, it was found that martensitic transformation occurs in porous NiTi alloys under a constant tensile load during cooling. The elongated temperature dependencies of the deformation accumulation and the deformation return are caused by the structural inhomogeneities of the porous alloys. The dependencies also indicate a redistribution of the chemical and nonchemical contributions to the driving force of martensitic transformation. The main contribution to the width of the temperature hysteresis and to the residual strain is made by plastic deformation caused by particles of secondary phases, non-metallic inclusions, and surface layers. The structural-phase inhomogeneity prevents the movement of interfacial martensitic boundaries, which is accompanied by the dissipation of thermal energy. In this case, structural-phase inhomogeneities of porous NiTi-(Ar) and NiTi-(N) alloys limit the accumulation of inelastic martensitic deformation to 1.3 and 0.7%, respectively. The presence of a larger proportion of oxynitride inclusions in the surface layer and the matrix of the porous NiTi-(N) alloy leads to a decrease in the proportion of the B2 phase. This is also the reason for the increase in irreversible permanent deformation and the width of the temperature hysteresis loop (Table 4).

Mechanical properties were studied by uniaxial tension of porous NiTi-(Ar) and NiTi-(N) samples (Figure 13a). Regardless of the SHS gas atmosphere, the fracture of all the samples occurred according to the brittle mechanism, but until the fracture moment, the strain hardening of porous alloys proceeded according to the elastoplastic mechanism. The elastoplastic mechanism was found when examining the destroyed interpore bridges of the porous framework (Figure 13b). No traces of plastic deformation in the form of constriction necks were found on the fractograms.

These results can be attributed to the fact that the main viscous phase of the NiTi matrix is surrounded by a brittle intermetallic surface layer and contains the brittle Ti<sub>2</sub>Ni phase. On the fracture surfaces there was found a pitting relief of viscous austenite TiNi(B2) fracture and areas of quasi-brittle cleavage of martensite TiNi(B19'), brittle cleavage of secondary phases Ti<sub>2</sub>Ni, Ti<sub>4</sub>Ni<sub>2</sub>O. The proportion of brittle fracture surfaces is much higher in NiTi-(N) specimens. Tensile NiTi-(Ar) specimens achieved correspondingly large values of maximum strain and developed forces. The tensile strength was about 250 MPa with a deformation of 1.9%. For NiTi-(N) alloys, all mechanical characteristics are noticeably lower than for NiTi-(Ar) alloys. The tensile strength of the NiTi-(N) alloy was about 190 MPa at 1.5% strain (Table 5). Despite the obvious qualitative differences in the fracture surfaces of the NiTi-(N) and NiTi-(Ar) specimens, the tension curves differ only quantitatively.

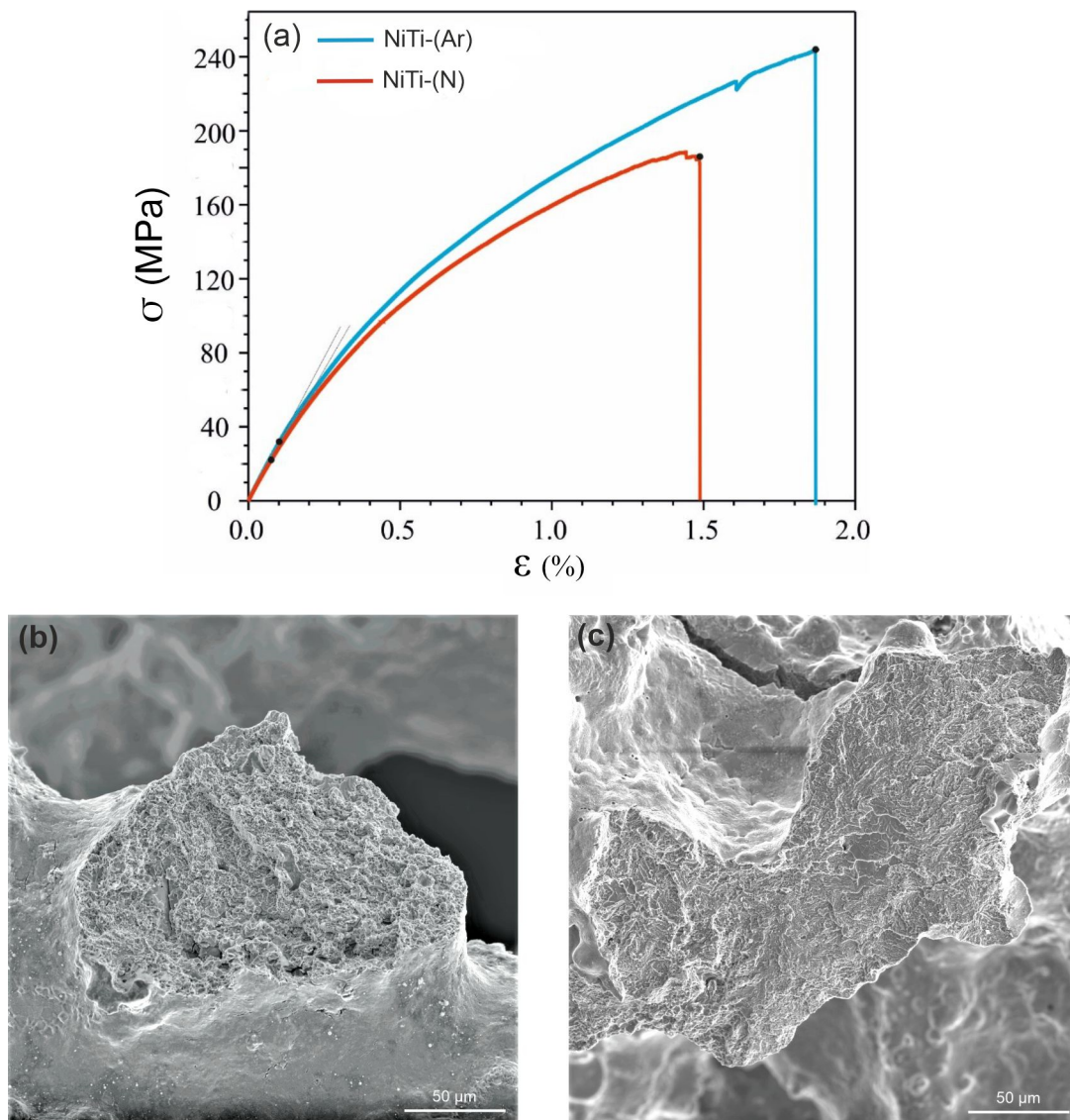


**Figure 13.** Deformation diagrams obtained during uniaxial tension of porous NiTi plates  $20 \times 12 \times 5 \text{ mm}^3$  in size (a), general view of the inter-pore bridge fractogram of the porous NiTi-(Ar) (b) and NiTi-(N) (c) plates.

**Table 5.** Mechanical properties of porous NiTi-(Ar) and NiTi-(N) samples.

Sample	$\sigma_y$ , MPa	$\sigma_B$ , MPa	$E$ , GPa	$\epsilon_{\max}$ , %
NiTi-(Ar)	$32 \pm 0.2$	$242 \pm 23$	$31 \pm 0.3$	$1.88 \pm 0.1$
NiTi-(N)	$22 \pm 0.2$	$187 \pm 17$	$31 \pm 0.4$	$1.49 \pm 0.1$

Here,  $\sigma_y$  is the elastic limit,  $\sigma_B$  is the ultimate tensile strength,  $E$  is the modulus of elasticity,  $\epsilon_{\max}$  is the maximum deformation before fracture.

Thus, the synthesis gaseous atmosphere is shown to affect the elastic limit, ultimate strength and maximum tensile strain of the porous framework.

#### 4. Conclusions

- The results of the XRD and EBSD analyses showed that the porous NiTi-(N) alloy is characterized by an increase in the volume fraction of brittle interstitial  $\text{Ti}_4\text{Ni}_2\text{O(N)}$  phases and an appearance of a finely dispersed  $\text{TiNi}_3$  phase. The increase in the

proportion of the  $Ti_4Ni_2O(N)$  phase as well as the increased nitrogen content in the surface layer found in the NiTi-(N) alloy favorably affect the cytocompatibility of the surface with bone marrow mesenchymal cells. The percentage of the cells covering the surface of NiTi-(N) is high and accounts for 90%, in contrast to NiTi-(Ar) where the percentage of the cell coverage is 75%.

2. DSC analysis shows that the reversible martensitic transition  $B2 \leftrightarrow B19'$  is typical of these two alloys and the gaseous atmosphere does not affect the characteristic martensitic transformation temperatures during cooling and heating without load. However, the study of martensitic transformation under load during SME showed a significant difference in the deformation behavior of porous NiTi-(Ar) and NiTi-(N) alloys. It has been established that the austenitic B2 phase in porous NiTi-(Ar) alloys accumulates up to 1% deformation while cooling, and in porous NiTi-(N) alloys it does not exceed 0.5%. It was found that there is an increase in the width of the temperature hysteresis and irreversible deformation in NiTi-(N) alloy.
3. Uniaxial tension of porous NiTi-(Ar) and NiTi-(N) plates to fracture showed that the alloys are characterized by an elastic–plastic mechanism of strain hardening. A large proportion of brittle fracture areas was found on the fractograms of the NiTi-(N) alloy, which indicates the presence of a larger volume fraction of brittle  $Ti_2Ni + Ti_4Ni_2O(N)$  phases. All mechanical characteristics of NiTi-(N) alloys are noticeably lower than those of NiTi-(Ar) alloys. The ultimate strength of the NiTi-(Ar) alloy was 250 MPa, whereas that of the NiTi-(N) alloy was 190 MPa.
4. Thus, according to the data obtained, porous NiTi-(N) alloys under low physiological load can be considered more biocompatible. To use porous NiTi-(N) alloys under high physiological load, it is necessary to increase their reversible deformation value and tensile strength.

**Author Contributions:** Conceptualization, E.M., G.B. and A.S.; methodology, E.M., G.B. and A.S.; investigation, E.M., G.B. and A.S.; formal analysis, G.B. and A.S.; resources, E.M. and G.B.; Writing—Original draft preparation, G.B., E.M. and A.S.; Writing—Review and editing, E.M., A.S. and G.B.; supervision, E.M. and G.B.; project administration, G.B; funding acquisition, G.B. and E.M. All authors have read and agreed to the published version of the manuscript.

**Funding:** This study was supported by the Tomsk State University Development Programme (Priority-2030).

**Institutional Review Board Statement:** Not applicable.

**Informed Consent Statement:** Not applicable.

**Data Availability Statement:** Not applicable.

**Acknowledgments:** The structure research was carried out with the equipment of Tomsk Regional Core Shared Research Facilities Center of National Research Tomsk State University (Grant of the Ministry of Science and Higher Education of the Russian Federation no. 075-15-2021-693 (no. 13.RFC.21.0012)).

**Conflicts of Interest:** The authors declare no conflict of interest.

## References

1. Wisutmethangoon, S.; Denmud, N.; Sikong, L. Characteristics and compressive properties of porous NiTi alloy synthesized by SHS technique. *Mater. Sci. Eng. A* **2009**, *515*, 93–97. [[CrossRef](#)]
2. Saedi, S.; Saghaian, S.E.; Jahadakbar, A.; Moghaddam, N.S.; Andani, M.T.; Saghaian, S.M.; Lu, Y.C.; Elahinia, M.; Karaca, H.E. Shape memory response of porous NiTi shape memory alloys fabricated by selective laser melting. *J. Mater. Sci. Mater. Med.* **2018**, *29*, 1–12. [[CrossRef](#)] [[PubMed](#)]
3. Zhang, L.; Zhang, Y.Q.; Jiang, Y.H.; Zhou, R. Superelastic behaviors of biomedical porous NiTi alloy with high porosity and large pore size prepared by spark plasma sintering. *J. Alloys Compd.* **2015**, *44*, 513–522. [[CrossRef](#)]
4. Sevilla, P.; Aparicio, C.; Planell, J.A.; Gil, F.J. Comparison of the mechanical properties between tantalum and nickel-titanium foams implant materials for bone ingrowth applications. *J. Alloys Compd.* **2007**, *439*, 67–73. [[CrossRef](#)]

5. Ipek, N.G.; Dericioglu, A.F.; Bor, S. Fatigue behavior of TiNi foams processed by the magnesium space holder technique. *J. Mech. Behav. Biomed. Mater.* **2011**, *4*, 2017–2023. [[CrossRef](#)]
6. Nakas, G.I.; Aşık, E.E.; Tunca, B.; Bor, S. Fatigue and Fracture Behavior of Porous TiNi. *Alloys. Mater. Sci. Forum.* **2014**, *783*, 591–596. [[CrossRef](#)]
7. Yasenchuk, Y.; Marchenko, E.; Gunther, V.; Radkevich, A.; Kokorev, O.; Gunther, S.; Baigonakova, G.; Hodorenko, V.; Chekalkin, T.; Kang, J.H.; et al. Biocompatibility and clinical application of porous TiNi alloys made by self-propagating high-temperature synthesis (SHS). *Materials* **2019**, *12*, 2405. [[CrossRef](#)]
8. Marchenko, E.S.; Baigonakova, G.A.; Yasenchuk, Y.F.; Chekalkin, T.L.; Volinsky, A.A. Structure, biocompatibility and corrosion resistance of the ceramic-metal surface of porous nitinol. *Ceram. Int.* **2022**, *48*, 33514–33523. [[CrossRef](#)]
9. Starosvetsky, D.; Gotman, I. TiN coating improves the corrosion behavior of superelastic NiTi surgical alloy. *Surf. Coat. Technol.* **2001**, *148*, 268–276. [[CrossRef](#)]
10. Soltanalipour, M.; Khalil-Allafi, J.; Ghareshabani, E.; Khalili, V. Electrochemical behaviour of NiTi alloy coated with TiN using DPF. *Surf. Eng.* **2017**, *33*, 474–481. [[CrossRef](#)]
11. Novak, P.; Mejzlikova, L.; Michalcova, A.; Capek, J.; Beran, P.; Vojtech, D. Effect of SHS conditions on microstructure of NiTi shape memory alloy. *Intermetallics* **2013**, *42*, 85–91. [[CrossRef](#)]
12. Tay, B.Y.; Goh, C.W.; Gu, Y.W.; Lim, C.S.; Yong, M.S.; Ho, M.K.; Myint, M.H. Porous NiTi fabricated by self-propagating high-temperature synthesis of elemental powders. *J. Mater. Process. Technol.* **2008**, *202*, 359–364. [[CrossRef](#)]
13. Li, B.Y.; Rong, L.J.; Li, Y.Y.; Gjunter, V.E. Synthesis of porous Ni–Ti shape-memory alloys by self-propagating high-temperature synthesis: Reaction mechanism and anisotropy in pore structure. *Acta Mater.* **2000**, *48*, 389–3904. [[CrossRef](#)]
14. Novak, P.; Vesely, T.; Marek, I.; Dvorak, P.; Vojtech, V.; Salvetr, P.; Hausild, P.; Kopecek, J. Effect of Particle Size of Titanium and Nickel on the Synthesis of NiTi by TE-SHS. *Metall. Mater. Trans. B.* **2016**, *47*, 932–938. [[CrossRef](#)]
15. Resnina, N.; Rubanik, V., Jr.; Rubanik, V.; Kulak, M.; Belyaev, S.; Liulchak, P.; Chepela, D.; Kalganov, V. Influence of the Ar pressure on the structure of the NiTi foams produced by self-propagating high-temperature synthesis. *Mater. Lett.* **2021**, *299*, 130047. [[CrossRef](#)]
16. Novak, P.; Kadlecova, B.; Salvetr, P.; Knaislova, A.; Skolakova, A.; Karlik, M.; Kopecek, J. Effect of Reaction Atmosphere and Heating Rate During Reactive Sintering of Ni–Ti Intermetallics. *Procedia Eng.* **2017**, *184*, 681–686. [[CrossRef](#)]
17. Gunther, V.; Yasenchuk, Y.; Chekalkin, T.; Marchenko, E.; Gunther, S.; Baigonakova, G.; Hodorenko, V.; Chekalkin, T.; Kang, J.H.; Weiss, S.; et al. Formation of pores and amorphous-nanocrystalline phases in porous TiNi alloys made by self-propagating high-temperature synthesis (SHS). *Adv. Powder Technol.* **2019**, *30*, 673–680. [[CrossRef](#)]
18. Balogh, Z.; Schmitz, G. *Physical Metallurgy*, 1st ed.; Laughlin, D.E., Hono, K., Eds.; Elsevier: Pittsburgh, PA, USA, 2015; pp. 387–559.
19. Zeng, K.; Schmid-Fetzer, R.; Rogl, P. A thermodynamic analysis of cermet sintering of TiN–Ni powder mixtures. *J. Phase Equilib.* **1997**, *19*, 124–135. [[CrossRef](#)]
20. Massalski, T.B.; Okamoto, H.; Subramanian, P.R.; Kacprzak, L. *Binary Alloy Phase Diagrams*, 2nd ed.; ASM International: Novelty, OH, USA, 1990; p. 3589.
21. Qiu, A.T.; Liu, L.J.; Pang, W.; Lu, X.G.; Li, C.H. Calculation of phase diagram of Ti–Ni–O system and application to deoxidation of TiNi alloy. *Trans. Nonfer. Met. Soc. China* **2011**, *21*, 1808–1816. [[CrossRef](#)]
22. Mehrer, H. *Diffusion in Solid Metals and Alloys*; Springer: Berlin/Heidelberg, Germany, 1990; p. 752.
23. Vykhodets, V.B.; Klotsman, S.M.; Kurennykh, T.Y.; Levin, A.D.; Pavlov, V.A. Diffusion of oxygen in  $\alpha$ -Ti. V. temperature dependence coefficients of oxygen diffusion. *Phys. Met. Metallogr.* **1989**, *68*, 94–97.
24. Kaya, M.; Orhan, N.; Kurt, B.; Khan, T.I. The effect of solution treatment under loading on the microstructure and phase transformation behavior of porous NiTi shape memory alloy fabricated by SHS. *J. Alloys Compd.* **2009**, *475*, 378–382. [[CrossRef](#)]
25. Jiang, H.C.; Rong, L.J. Ways to lower transformation temperatures of porous NiTi shape memory alloy fabricated by self-propagating high-temperature synthesis. *Mater. Sci. Eng. A* **2006**, *438*, 883–886. [[CrossRef](#)]
26. Zu, X.T.; Zhang, C.F.; Zhu, S.; Huo, Y.; Wang, Z.G.; Wang, L.M. Electron irradiation-induced changes of martensitic transformation characteristics in a TiNiCu shape memory alloy. *Mater. Lett.* **2003**, *57*, 2099–2103. [[CrossRef](#)]